Rakenteiden Mekaniikka (Journal of Structural Mechanics)
Vol. 42, No 1, 2009, pp. 1-37

Experimental and Numerical Studies on Projectile Impacts

Arja Saarenheimo, Markku Tuomala, Kim Calonius, Ilkka Hakola, Simo Hostikka and Ari Silde

Abstract. Aircraft impact is considered as a relevant loading case in designing modern nuclear power plants. Numerical methods and models need to be verified against experimental data in order to guarantee the reliability of results when simulating full scale applications. The IMPACT test facility has been developed starting in 2003 and is has reached a mature phase where well repeatable tests can be conducted and broad range of dynamic data acquired reliably.

Keywords: Impact loaded reinforced concrete structures, liquid spreading, fire dynamics simulation

Introduction

In order to obtain reliable numerical results the used methods and models should be verified against experimental data. The objective of this paper is to study the accuracy and capability of numerical methods in analysing reinforced concrete structures under soft missile impacts.

Numerical studies are carried out by a multi purpose code Abaqus [1] using shell element models for both the target and the missile. Simplified two degree of freedom models can be used in preliminary design of real protective structures and also in designing experiment. Due to uncertainties in measuring the force-time functions for impacting missiles load functions needed in analyses were calculated by using the Riera method [2] and adjusted according to the experimental findings. Parameters for material models used in the analyses are based on the available material test data.

Impact test facility and measurements

A flexible experimental platform has been created at VTT for intermediate scale impact tests. The test apparatus consists of two main parts. First, a 13.5 m long pressure accumulator is used to provide the required initial energy for the test. Second, a 12 m long acceleration tube is used to accelerate test missiles to a final velocity of 100 m/s to 200 m/s. The test facility is shown in Figure 1. The mass of the missile can be up to 100 kg. In the tests, missile impacts on a concrete wall or on a steel force measurement plate. The test facility has been further developed and improved since the first version was taken in use in 2003.

Figure 1. Impact test facility (pressure pipe, acceleration tube, piston catcher and force plate or impact wall)

Two versions of the force plate system are shown in Figure 2. The force plates have been supported directly to bedrock using only the back pipes. The 3D missile tests were performed by using a heavy steel frame, horizontal beams and three force plates installed in front of the frame, depicted in Figure 2 on the right.

Figure 2. The second model (left) and third model of force plate construction.

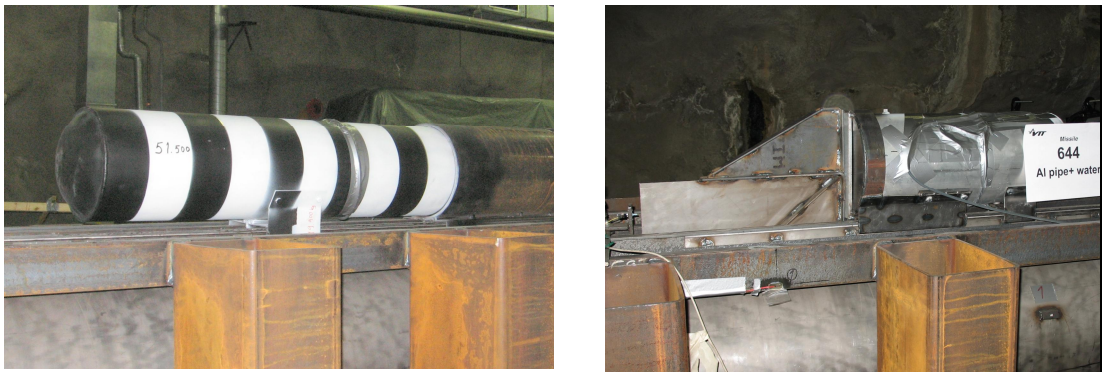

Figure 3. Dry (empty) aluminium (Al) pipe missile and wet (water filled) missile.

Tests have been done accelerating a steel piston inside the acceleration tube with the missile installed on the rails at the top of the acceleration tube. An aluminium pipe missile with a diameter of 0.25 m and wall thickness of 5 mm, shown in Figure 3, was used in impact tests of slabs with a thickness of 0.15 m. Tests with 3D missiles on force plate have been done using a smaller aluminium pipe, with a diameter of 200 mm and wall thickness of 4 mm. At the end of the test series wings and engines were included in the model, depicted in Figure 4, and also in some tests wings were filled with water in order to study the spreading of liquid [3].

Pre-stressed concrete slabs with a thickness of 250 mm were tested using rigid hard steel missiles with a diameter of 150 mm, wall thickness of 10 mm and filled with concrete, shown in Figure 4 on the left.

Figure 4. The rigid steel pipe missile with a diameter of 170 mm (left) and a 3D missile with wings (right).

The dimensions of the concrete slab in the soft missile tests were: width 2 m, length 2.3 m, support length 2.2 m and thickness 0.15 m. Bending and in some cases also shear reinforcement was applied. The slabs were supported on the vertical edges by the test frame, shown in Figure 5 on the left.

The pre-stressed concrete slabs were of the same size except the thickness was 0.25 m. In the new test frame the slabs are simply supported on all the four edges. The new test frame is shown in Figure 5 on the right.

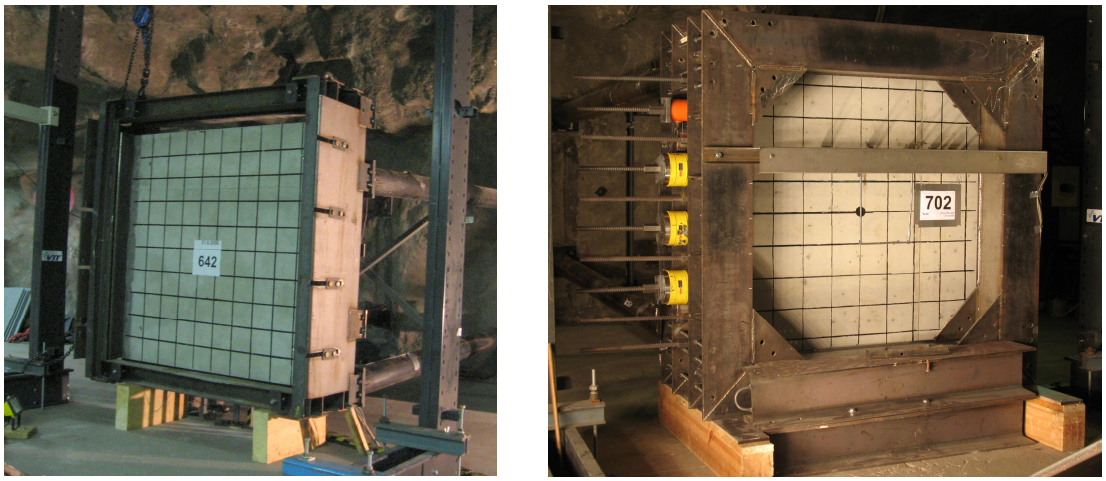

Figure 5. Support system and one-way test slab in a soft missile test (left). A pre-stressed test slab with a thickness of 0.25 m and support system 2 in hard missile tests (right).

The data from sensors have been gathered using a sampling frequency of 100 kHz. In measuring anti-aliasing filtering and simultaneous sampling was applied. The maximum number of channels used in the tests has been 32. The following sensors have been used in the impact tests:

- Force transducers behind the force plate (used also in measuring the post-tension force of Dywidag bars).
- Strain gauges on the back pipes to measure reaction forces.
- Strain gauges on the supporting frame to control the bending stresses of beams.
- High speed cameras to video collision.
- Strain gauges in rebars inside concrete to measure strains of rebars.
- Strain gauges on the surface of the concrete slab to measure strains of concrete.
- Deflection transducers to measure horizontal deflections of the slab.
- Laser sensors to measure the speed of missile.
- Accelerometer at the back of the missile (wired measurements).
- Accelerometers at the back of the concrete wall.
- Pressure sensors to measure the air pressure inside the acceleration tube or near the concrete slab.

The measuring device and deflection transducers are shown in Figure 6. The transducer is a mechanical sensor, which is fixed on the surface of the slab and it is also working during the test.

Figure 6. Measuring data collection device (left) and deflection transducers in front of the slab (right).

Load function of soft missile

One of the earliest studies on the calculation of load-time function of a deforming projectile was published in Reference [2], and the subject has been considered in several articles since, e.g. in [4].

The impact force $F(t)$ of a deforming or crushing projectile can be obtained from the change of momentum equation

$$F(t) = \frac{d}{dt}(M_r v_m), \tag{1}$$

in which M_r is the remaining mass of the missile and v_m is the velocity. By differentiation

$$F(t) = M_r \frac{dv_m}{dt} + v_m \frac{dM_r}{dt}. \tag{2}$$

As in Reference [2] crushing is assumed to take place at the missile/target interface and the crushing force is in equilibrium with the inertial force of the remaining mass M_r of the projectile

$$P_c = M_r \frac{dv_m}{dt}. \tag{3}$$

In the second term of (2)

$$\frac{dM_r}{dt} = -v_m m(x), \tag{4}$$

where $m(x)$ is the mass per unit length of the missile and x is the distance to the contact cross section measured from the nose of projectile. The impact force (2) becomes

$$F(t) = P_c(x(t)) - m(x(t))v_m^2(t). \tag{5}$$

Assuming that the mass of the crushed part of the missile moves with the target structure an equation for the conservation of momentum for the system of missile and target yields

$$F(t) = \frac{d}{dt}(M_r v_m + M_c v_t), \tag{6}$$

where M_r is the mass of the rigid (uncrushed part), M_c is the mass of the crushed part, v_m is the velocity of the rigid part of the missile at time t, v_t is the velocity of the target at time t.

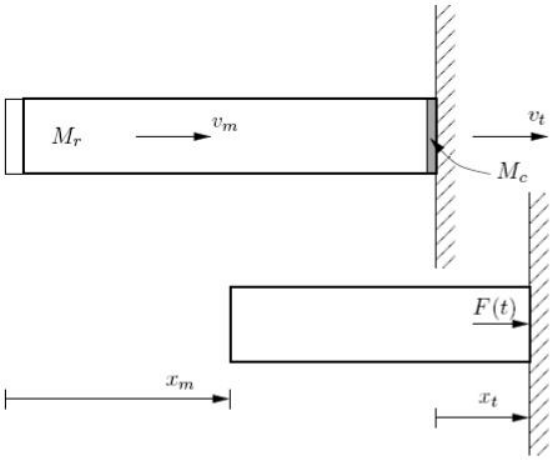

Figure 7. Impact of deforming missile.

The impact force formula in the case of deforming target becomes

$$F(t) = P_c(x(t)) - m(x(t))(v_m - v_t)^2 + M_c \frac{dv_t}{dt}. \tag{7}$$

The area on which the load resultant is distributed must be estimated separately based on the cross sectional area of the missile.

Given as initial values the mass distribution and the crushing strength (force) distribution as functions of the distance measured from the missile nose, the resultant load function can be calculated by time integration using the above equations.

In a simple way, the movement of the target can be given by an equation [5]

$$x(t) = u_{tm}(1 - \cos\frac{\pi}{2t_m}t), \tag{8}$$

where u_{tm} is the amplitude of target movement at the end of the impact at time t_m.

Crushing force

Various crushing force formulae for tubes with different cross sections under static, quasi-static and slow dynamic loading for different applications, e.g. in automotive industry, have been derived and given in literature. Alexander [6] has derived by a plastic mechanism method an approximate solution for the crushing force of a thin-walled circular tube by assuming an axisymmetric mode of deformation, depicted in Figure 8, [7]. It is assumed that the tube is made of a rigid plastic material. The assumed mode of deformation or collapse mode is an idealisation because in reality the wrinkles are curved.

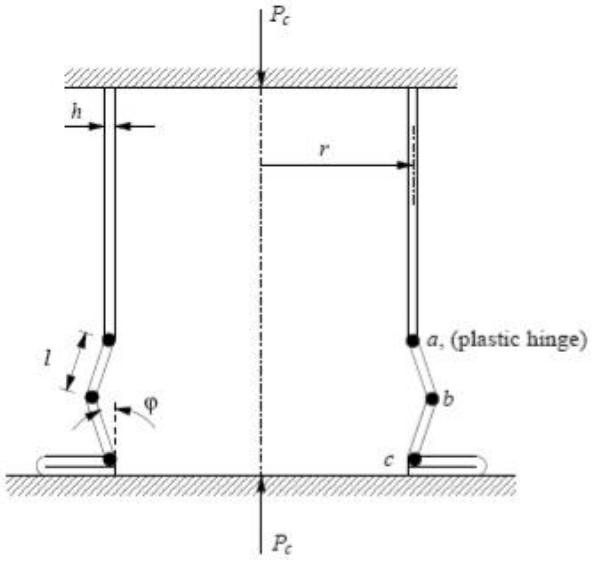

Figure 8. Folding mechanism.

The external work needed to develop and flatten one axisymmetric wrinkle is equated with the internal energy dissipated in plastic deformation in the tube. The plastic internal work is generated at hinge lines *a* and *c* and at the moving hinge line *b*. Third portion of the internal work comes from the stretching of tube portions *ab* and *bc*.

The work equation yields the crushing force

$$P_c = \pi h[h(\pi r / l + 1)/\sqrt{3} + l]\sigma_m, \tag{9}$$

where r and h are the radius and the wall thickness of the tube, respectively, and the length parameter l is shown in Figure 8.

Minimising the axial crushing force P_c with respect to the length parameter l gives

$$l = \sqrt{\frac{\pi r h}{\sqrt{3}}} \approx 1.347\sqrt{rh}, \tag{10}$$

and the minimum value for P_c becomes

$$\frac{P_c}{m_p} = 4(3)^{1/4}\pi^{3/2}\sqrt{\frac{r}{h}} + 2\pi, \tag{11}$$

which is the same as Alexander's solution, [7]. In equation (11) the plastic bending moment capacity of the tube wall with a thickness h and a yield stress σ_y is

$$m_p = \frac{2}{\sqrt{3}}\sigma_y \frac{h^2}{4}, \tag{12}$$

assuming the von Mises yield condition and a state of plane strain.

The Cowper-Symonds constitutive equation for uniaxial tension or compression is [7]

$$\sigma_{yd} = \sigma_y\left[1 + \left(\frac{\dot{\varepsilon}}{D}\right)^{1/q}\right], \tag{13}$$

where σ_y and σ_{yd} are the static and the dynamic flow stress, respectively, and D and q are material parameters.

The average strain rate in the circumferential direction becomes, [7], $\dot{\varepsilon}_\theta = \frac{v_0}{4r}$, where v_0 is the axial velocity of projectile. Substituting this into the dynamic yield stress formula (12) and the crushing force formula gives

$$P_c = 2(\pi h)^{3/2}\sqrt{r}\,\sigma_y\left[1 + \left(\frac{v_0}{4rD}\right)^{1/q}\right] \Big/ 3^{1/4}. \tag{14}$$

A more refined solution for the crushing force is given in [7] in which the actual deformed shape of the tube is approximated more closely. Also the actual circumferential strain variation is used, instead of the average value, assumed in Alexander's solution, in calculating the stretching energy. In this solution approximately

$$l \approx 1.76\sqrt{\frac{rh}{2}} \approx 1.245\sqrt{rh} \tag{15}$$

in the range $10 \le 2r/h \le 60$, and the mean axial crushing load becomes

$$\frac{P_c}{m_p} = \frac{29.4\sqrt{\frac{r}{h}} + 11.9}{0.86 - 0.37\sqrt{\frac{h}{r}}}. \tag{16}$$

Soft missile impact tests

Some soft missile impact tests, reported in literature, are reviewed in the following. Impact force histories are calculated by the Riera method, and the portion of the crushing force is identified.

Phantom impact test at Sandia

In a full scale test, reported in [8], a Phantom fighter, supported by a sledge and powered by rockets, was run onto a concrete block, with an impact velocity of 215 m/s. The fighter was completely destroyed into pieces only with a small reduction of velocity. The weight of the concrete block was 25 times the weight of the fighter. The concrete block was supported on the ground nearly without friction. The impact force could be evaluated from the formula

$$F(t) = M_b a_b(t), \tag{17}$$

where M_b is the mass of the concrete block and $a_b(t)$ is its acceleration as measured in the test at time t. The impact force was also measured directly with equipments installed in the fuselage. The impact force measured from the aeroplane is obtained from the formula

$$F(t) = M_r \frac{dv}{dt} + \alpha m(x(t))(v - v_b)^2, \tag{18}$$

where M_r is again the mass of the still uncrushed part of the aircraft and v is its velocity, $m(x(t))$ is the value of the mass distribution at time t in the cross section $x=x_c$ in contact with the target, v_b is the velocity of the concrete block and α is a coefficient of effective mass. Based on the measurements in [8] for the case of Phantom a value $\alpha = 0.9$ is adopted.

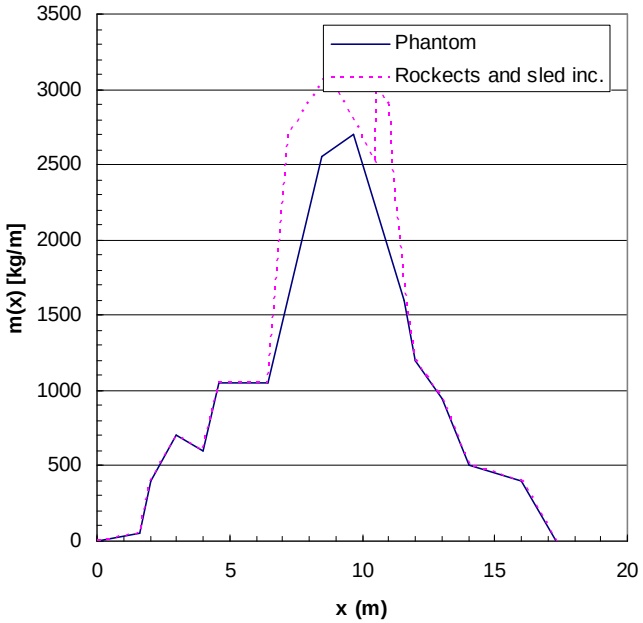

Figure 9. Mass distribution of Phantom.

Distributions for $m(x)$ and $P_c(x)$, with slight simplifications, based on figures shown in [8] are used in the present calculations. The resultant load function for Phantom is shown in Figure 10 with the crushing force distribution, P_c, of [8].

The effect of target deflection is studied by assuming a deflection value u_{tm} = 0.4 m at time t_m = 0.088 s.

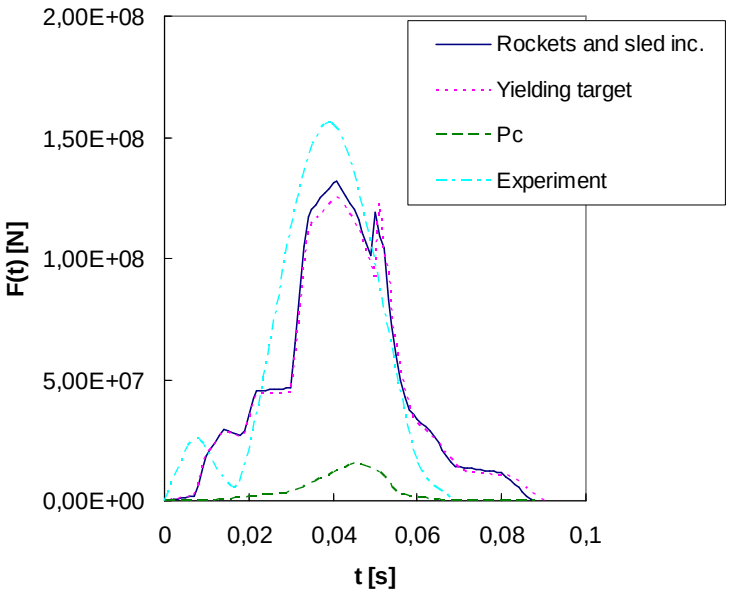

Figure 10. Impact force of Phantom.

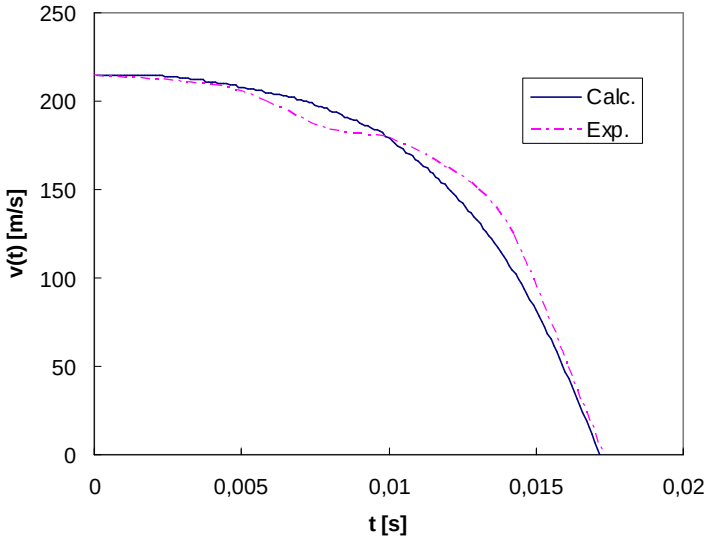

Figure 11. Velocity reduction curve of engine GE-J79.

Phantom engine impact tests

In Reference [9] experiments by using different projectiles, both rigid and deformable with different masses, have been made. Large scale missile (LED) had a mass of 1500 kg and a diameter of 0.76 m. Also the full scale engine GE-J79 of Phantom was used as projectile. The mass of the engine was evaluated by immersing it gradually in water. Also the crushing force of GE-J79 was determined experimentally in [10]. The impact force calculated by using the data of [9] is shown in Figure 12. The result is quite similar to the impact force distribution determined in [10] based on the measured velocity reduction curve and the mass distribution of the engine. A smoothed velocity reduction curve of Reference [10] together with the corresponding calculated curve is shown in Figure 11. The peak force in [10] was 52 MN and the impact duration was 17 ms.

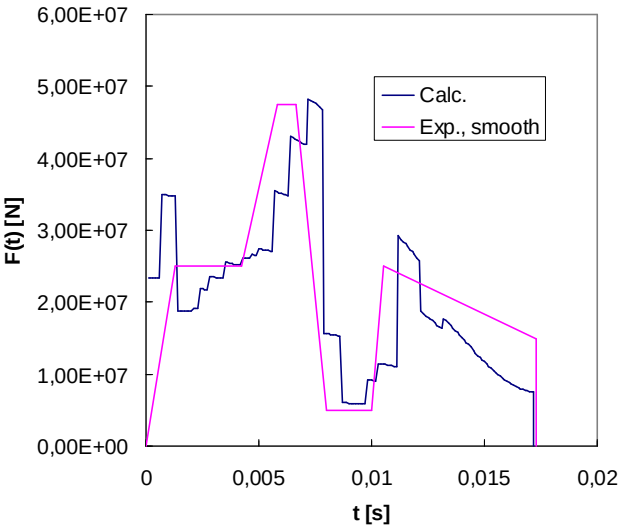

Figure 12. Impact force of engine GE-J79.

Steel pipe projectile

Consider a circular cylindrical steel pipe missile with the following dimensions: diameter d=0.268 m (measured from axis to wall centre), wall thickness h=0.005 m or 5 mm and length L=0.91 m.

The front end of the missile was closed with a circular plate having a thickness of 5 mm and with a mass of about 2.21 kg. In the following calculations by the Riera method [2] the plate of the front end is not taken into account. The discrete longitudinal stiffener is smeared symmetrically to the pipe.

In the finite element analyses by axisymmetric shell elements the stress-strain curve consists of four linear parts. After attaining the strain value of 0.24 the uniaxial stress is assumed to remain constant at 340 MPa.

In a test the steel pipe missile of about 41 kg obtained an impact velocity of 121 m/s. The calculated impact force history is shown in Figure 16. The impact force is calculated by a visco-plastic folding mechanism model. The yield stress of missile material is assumed as 235 MPa. The viscoplastic parameters are D = 40.4 1/s and q = 5.

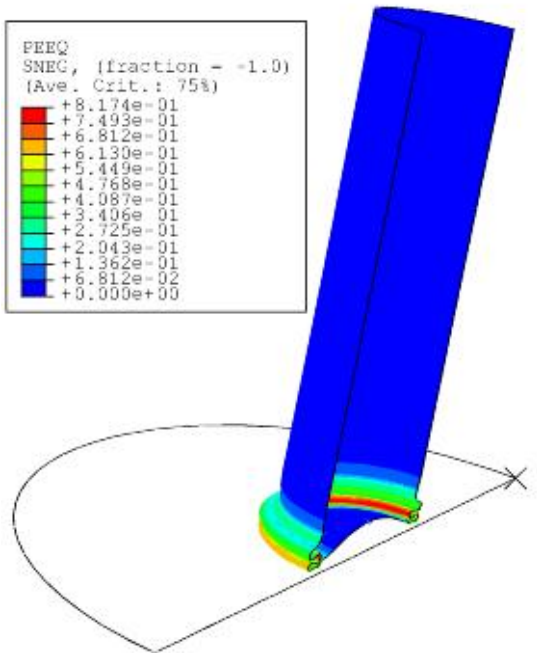

Figure 13. Deformed steel projectile with plastic strain.

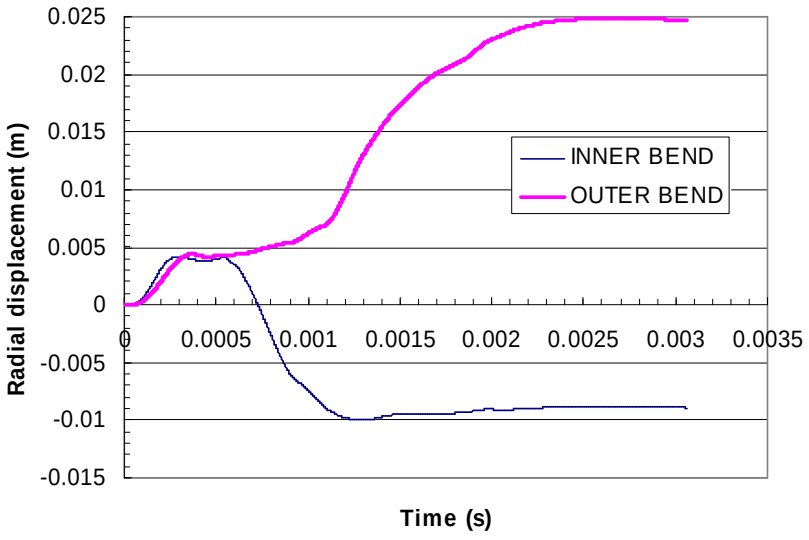

Figure 14. Radial displacement at the inner and outer bends of a wrinkle.

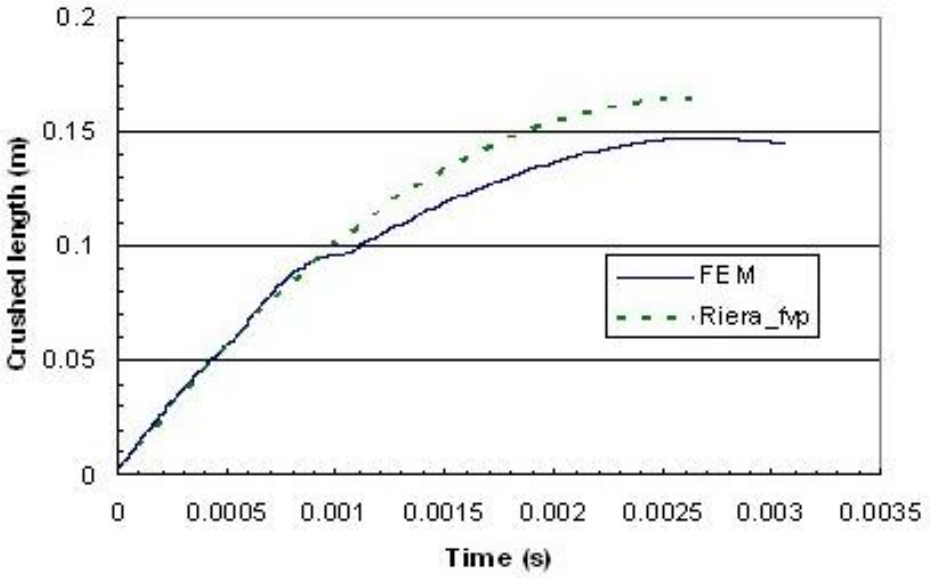

Figure 15. Crushed length of the steel missile.

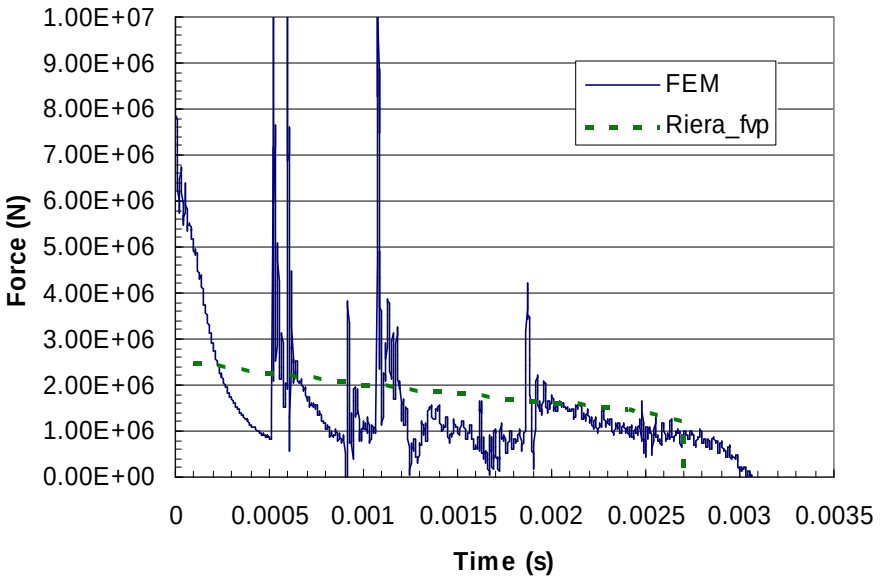

Figure 16. Impact force of the steel missile.

The deformed axisymmetric shape of a FE-model for the missile with a mass of 41 kg is shown in Figure 13 with the equivalent plastic strain contours at the inner surface of the pipe. This numerically simulated deformed shape corresponds well to the shape of the missile after the test, shown in Figure 17. The measured increase of the missile radius was about 24 mm. The radial displacements at the inner and outer bends of a

wrinkle are shown in Figure 14. The displacement recorded at the outer bend corresponds well to the measured value. The inner bend of a wrinkle deforms inwards about 10 mm and a value of 35 mm can be obtained for the wrinkle width. The same value can be obtained also using the analytic formula (10).

The missile crushed length and the impact force calculated by FEM and by the Riera method are shown in Figures 15 and 16. The measured crushed length of the deformed missile after the test was about 17 cm.

Figure 17. Steel missile after impact test.

Structural integrity analyses

Simplified methods

In order to study both bending and shear failure of a plate or shell impacted by a missile at least a two degree of freedom model (TDOF model) is needed, such as e.g. the CEB model of Reference [11]. In Figure 18 spring 1 and mass 1 are connected to the global bending deformation of the plate while spring 2 and mass 2 are used in modelling the local shear behaviour in the neighbourhood of missile impact area.

The behaviour of element 1 (bending spring) is shown in Figure 18 and the local behaviour connected with the possible formation of a shear cone (shear spring) is shown in Figure 19. The internal force in spring 2 is composed of the contributions due to concrete, r_c, stirrups, r_s, and bending reinforcement, r_b. Concrete behaves elastically until the displacement difference $u_{21}=u_2-u_1$ reaches the value u_{cu}. Stirrups are assumed to break when the difference is $u_{21}=u_{su}$. The ultimate displacement connected to concrete deformation u_{cu} is very small but usually a large displacement difference is needed to activate a significant bending reinforcement contribution to the shear spring force. The bending reinforcement breaks when $u_{21}=u_{bu}$.

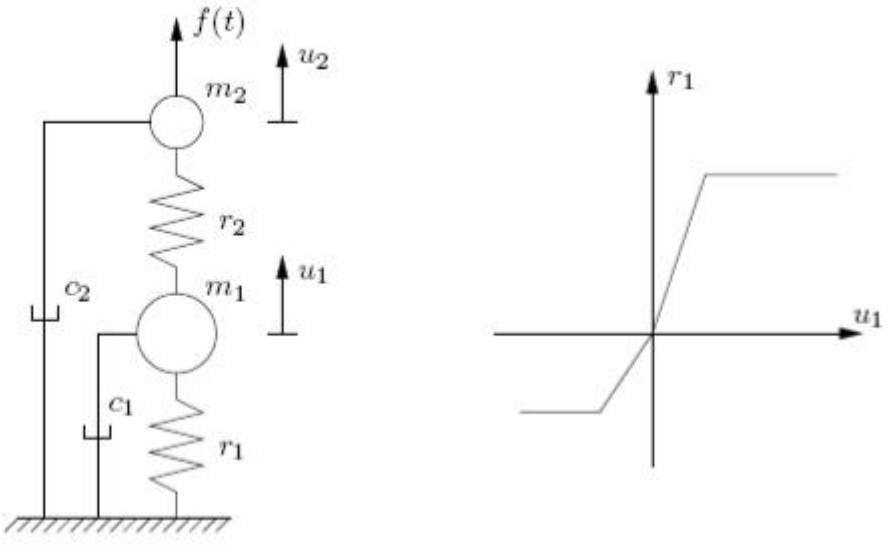

Figure18. A two degree of freedom (TDOF) impact model [11].

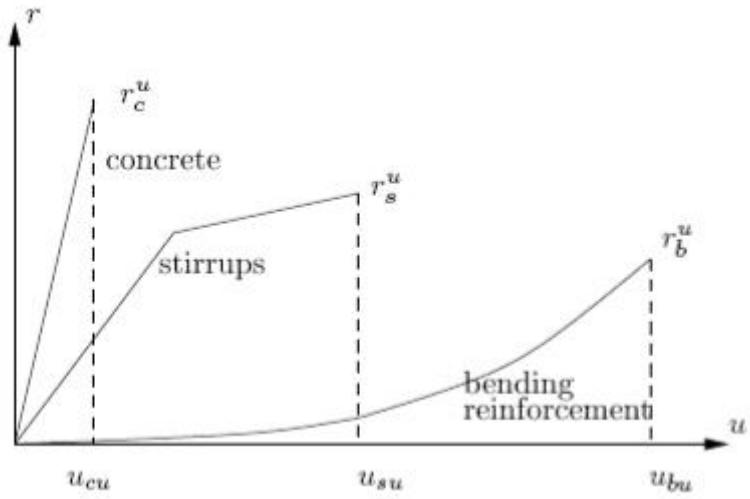

Figure 19. Local shear strength of slab model [11] showing the contributions of concrete, stirrups and bending reinforcement.

Stiffness, strength and effective mass of bending mode

In cracked state when concrete (in compression) and reinforcing steel still behave elastically a bending rigidity coefficient can be determined by assuming a triangular concrete stress distribution over a top compressed zone with a depth of x. If d is the effective slab depth (from top) and the distance from the neutral axis to the bending reinforcement is $d - x$, then one obtains

$$D = \left(d - \frac{x}{3} \right)(d - x) A_s E_c \tag{19}$$

for the bending stiffness per unit width of cross section, where A_s is the reinforcement area and E_s is the modulus of elasticity of steel.

Denoting the ratio $n = E_s/E_c$, where E_c is the modulus of elasticity of concrete, horizontal equilibrium equation in the absence of axial load gives

$$x = -nA_s \pm \sqrt{n^2 A_s^2 + 2nA_s d} \tag{20}$$

The reinforcement ratio is defined as

$$\rho_s = \frac{A_s}{d}. \tag{21}$$

If the top (t) and bottom (b) bending reinforcements are different, then the above values for x and D are determined for the loading direction, x_b and D_b, and for the opposite direction, x_t and D_t.

Also the limit load and effective mass are needed for the equations of motion of the TDOF system.

For a simply supported one-way slab with a width of B and with a span of L the bending spring stiffness becomes

$$k_b = \frac{48DB}{L^3}. \tag{22}$$

The limit load obtained with a central yield line is for this slab

$$R_p = \frac{4m_p B}{L}. \tag{23}$$

Denoting in the plate cross section the depth of the compressed zone a the equilibrium equations 0.85afc = Asfy and mp = Asfy(d-a/2) yield for the plastic bending moment

$$m_p = \rho_s d^2 f_y \left(1 - \frac{\rho_s f_y}{1.7 f_c} \right), \tag{24}$$

where f_y is the yield stress of steel, f_c is the compression strength of concrete and ρ_s is the reinforcement ratio.

The effective mass calculated with a piecewise linear deflection profile becomes

$$m_e = \frac{1}{3} \rho hlb. \tag{25}$$

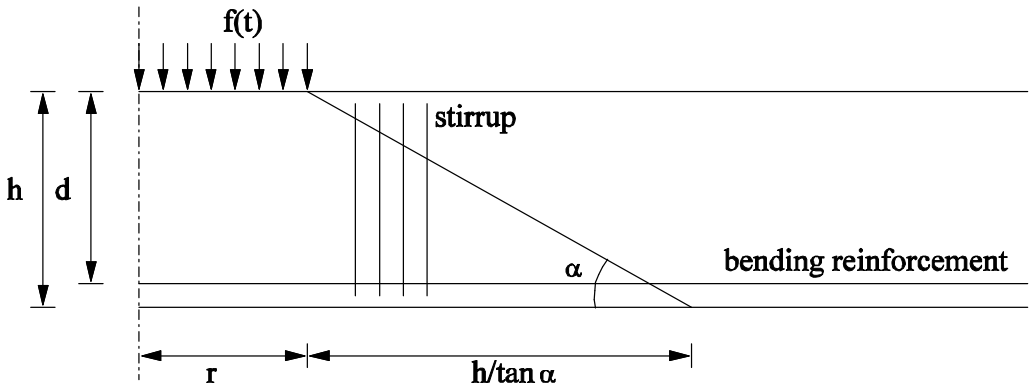

Figure 20. Assumed shear punching cone.

The local resistance of the slab to impact load is due to concrete, stirrups and bending reinforcement. The resistive force of concrete alone can be determined by assuming a shear cone with an angle of inclination of α measured from horizontal plane. If f_t is the tension strength of concrete, then

$$r_c^u = \pi\left[\left(r + \frac{h}{\tan\alpha}\right)^2 - r^2\right] f_t. \tag{26}$$

The ultimate cone displacement in the concrete deformation mode can be assumed as [11]

$$u_{cu} = \frac{1}{3}\frac{f_t}{E_c} h, \tag{27}$$

where h is the plate thickness. The ultimate resistive force and cone displacement due to stirrups is determined in a similar way, and it yields

$$r_s^u = \pi\left[\left(r + \frac{h}{\tan\alpha}\right)^2 - r^2\right] A_{ss} f_{sy}, \tag{28}$$

where A_{ss} is the amount of stirrups [m^2/m^2] and f_{sy} is the yield stress of stirrups. The ultimate elastic displacement due to stirrup deformation is assumed as

$$u_{se} = \frac{1}{3}\frac{f_{sy}}{E_s} h\,. \tag{29}$$

The ultimate cone displacement due to the deformation of stirrups is assumed as [11]

$$u_{su} = 0.9\varepsilon_{su} h, \tag{30}$$

where ε_{su} is the ultimate stirrup strain.

The contribution of the bending reinforcement to the shear resistance of the punching cone can be assessed by assuming a parabolic local deflection mode [11]

$$w(x) = u\left[1-\left(\frac{x}{a}\right)^2\right], \tag{31}$$

where $u = u_{21}$ and $x \in [0, a]$, $a = r + h/\tan\alpha$, for the bending reinforcement net. An average strain in the reinforcement bar due to bending is

$$\varepsilon = \frac{s-a}{a} = \frac{s}{a} - 1, \tag{32}$$

where s is the length of reinforcement bar in the deformed state. The arc length is calculated from

$$s = \int_0^a \sqrt{1+\left(\frac{dw}{dx}\right)^2}\,dx = \frac{a}{2}\sqrt{1+\left(\frac{2u}{a}\right)^2} + \frac{a^2}{4u}\ln\left[\frac{2u}{a} + \sqrt{1+\left(\frac{2u}{a}\right)^2}\right]. \tag{33}$$

The average strain in reinforcement bar becomes

$$\varepsilon = \frac{1}{2}\left\{\sqrt{1+\left(\frac{4u}{l}\right)^2} + \frac{l}{4u}\ln\left[\frac{4u}{l} + \sqrt{1+\left(\frac{4u}{l}\right)^2}\right]\right\} - 1, \tag{34}$$

where $l=2a$ is the bottom diameter of the shear cone, i.e. the diameter of area where the parabolic deflection mode is assumed.

In an isotropically reinforced plate the membrane force per unit length would be

$$t = A_s\sigma(\varepsilon), \tag{35}$$

where A_s is the amount of bending reinforcement.

The total vertical component of this inclined membrane force calculated from a circular line with a radius of a is

$$r_b = 2\pi a t \sin\varphi = \pi \sin\varphi l A_s \sigma(\varepsilon), \tag{36}$$

where φ is the angle of inclination of the bent reinforcement bar at a distance of a from the centre point, i.e.

$$\frac{dw}{dx}(a) \approx \varphi = \arctan\frac{2u}{a}. \tag{37}$$

In the Reference [11] a slightly different formula for the resistive force due to bending reinforcement is

$$r_b = 2\sin\left(\arctan\frac{4u}{l}\right) A_s \sigma(\varepsilon). \tag{38}$$

The mass of the assumed punching cone is

$$m_2 = \tilde{\rho}\pi h\left[a^2 + \frac{ah}{\tan\alpha} + \frac{1}{3}\left(\frac{h}{\tan\alpha}\right)^2\right], \tag{39}$$

where $\tilde{\rho}$ is the equivalent density of reinforced concrete, α is the angle of the punching cone (measured from horizontal plane) and h is the plate thickness.

The mass number 1 in the TDOF model is

$$m_1 = m_e - m_2. \tag{40}$$

Damping

The critical damping for a single degree of freedom (SDOF) model is

$$c_{cr} = 2\sqrt{km}, \tag{41}$$

where k and m are the stiffness coefficient and the mass of the model. Damping coefficients for the TDOF model are defined in [11] as

$$c_1 = \varsigma_1 2\sqrt{m_e k_b}, \tag{42}$$

$$c_2 = \varsigma_2 2\sqrt{m_2 k_{sc}}, \tag{43}$$

where $k_{sc}=r_{cu}/u_{cu}$ and the coefficients are in the ranges, $\varsigma_1 \in [0.02, 0.1]$ and $\varsigma_2 \in [0.005, 0.01]$. However, this definition of damping does not usually lead to the classical, proportional Rayleigh damping.

In this case the equations of motion are

$$m_1\ddot{u}_1 + c_1\dot{u}_1 - r_2 + r_1 = 0\,, \tag{44}$$

$$m_2\ddot{u}_2 + c_2\dot{u}_2 + r_2 = f\,, \tag{45}$$

where f is the load, r_1 and r_2 are the internal forces and the damping forces are

$$g_i = c_1\dot{u}_1, \quad g_2 = c_2\dot{u}_2. \tag{46}$$

In classical Rayleigh damping the damping matrix is assumed to be proportional to the mass matrix and the stiffness matrix in the form

$$\mathbf{C} = \alpha\mathbf{M} + \beta\mathbf{K}, \tag{47}$$

where α and β are constants used to control damping.

For an elastic structure, by modal decomposition, n independent equations are obtained in the form

$$m_i\ddot{u}_i + c_i\dot{u}_i + k_i u_i = f_i, \quad i = 1,...,n, \tag{48}$$

where m_i, c_i and k_i are the modal mass, damping and stiffness coefficients and n is the number of degrees of freedom in the system. The damping coefficient for equation i in the case of mass and stiffness proportional damping is

$$c_i = \alpha m_i + \beta k_i. \tag{49}$$

Taking $c = \zeta c_{cr} = \zeta 2\sqrt{km} = 2\zeta\omega m$, where $\omega = \sqrt{k/m}$ is the frequency, gives for mode i from (49)

$$2\zeta_i\omega_i = \alpha + \beta\omega_i^2 \tag{50}$$

and the modal damping ratio is obtained as

$$\zeta_i = \frac{\alpha}{2\omega_i} + \beta\frac{\omega_i}{2}. \tag{51}$$

Requiring that at two frequencies, $\omega = \omega_a$ and $\omega = \omega_b$, the damping ratios are ζ_a and ζ_b gives for the constants α and β

$$\alpha = \frac{2(\zeta_a\omega_b - \zeta_b\omega_a)}{\frac{\omega_b}{\omega_a} - \frac{\omega_a}{\omega_b}} \tag{52}$$

and

$$\beta = \frac{2(\zeta_a \omega_a - \zeta_b \omega_b)}{\omega_a^2 - \omega_b^2}. \tag{53}$$

In damped vibration

$$\omega_D = \omega\sqrt{1-\zeta^2}. \tag{54}$$

For the TDOF system the Rayleigh damping matrix is

$$\begin{bmatrix} C_{11} & C_{12} \\ C_{21} & C_{22} \end{bmatrix} = \begin{bmatrix} \alpha m_1 + \beta(k_1 + k_2) & -\beta k_2 \\ -\beta k_2 & \alpha m_2 + \beta k_2 \end{bmatrix}. \tag{55}$$

The equations of motion become

$$m_1 \ddot{u}_1 + g_1 - r_2 + r_1 = 0, \tag{56}$$

$$m_2 \ddot{u}_2 + g_2 + r_2 = f\ . \tag{57}$$

In this case the damping forces are

$$g_1 = c_{11}\dot{u}_1 + c_{12}\dot{u}_2 \tag{58}$$

and

$$g_2 = c_{21}\dot{u}_1 + c_{22}\dot{u}_2. \tag{59}$$

Due to mass m_e in (42) the mechanical model is not exactly the same as in Figure 18. The damping factor ς may be estimated from

$$\varsigma = \frac{\delta}{\sqrt{(2\pi)^2 + \delta^2}}. \tag{60}$$

The logarithmic decrement δ is

$$\delta = \frac{1}{n} \ln \frac{u_i}{u_{i+n}}, \tag{61}$$

in which u_i and u_{i+n} are two nonconsecutive amplitudes *n* cycles away.

For small values of ς, approximately

$$\delta = 2\pi\varsigma . \tag{62}$$

From the plot of a deflection-time recording from Test 642, considering vibration around the permanent deflection value, approximately $u_2 / u_3 \approx 5/3$ and $\varsigma \approx 0.08$ or using amplitudes u_1 and u_2 yields $\varsigma \approx 0.11$. A damping ratio value of 0.1 for lowest (bending) mode seems appropriate for the present application.

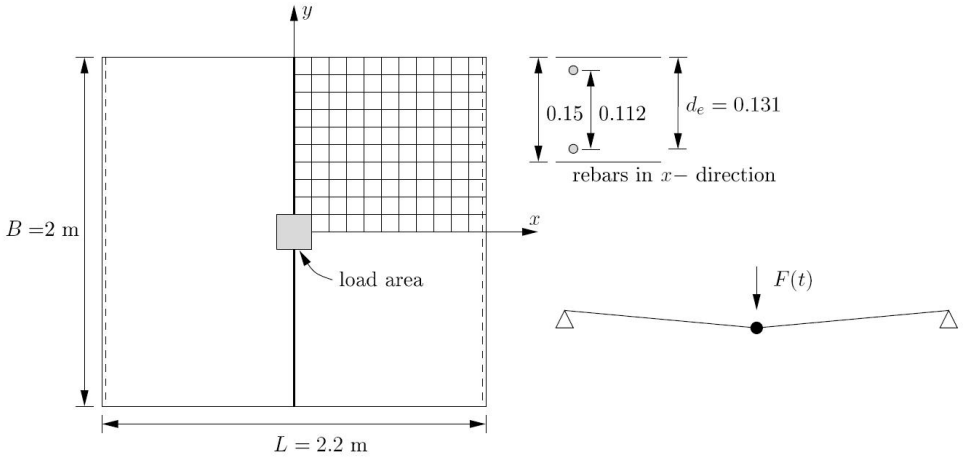

Figure 21. Reinforced concrete one-way slab impacted by a missile.

Aluminium missile with impact velocity 109 m/s

In the present series of projectile impact tests starting with Test 642 dry and wet aluminium missiles were shot on a reinforced concrete one-way target plate.

The dimensions of the slabs in the test series were: width 2 m, length 2.3 m, support length 2.2 m and thickness 0.15 m. The slab was simply supported on two opposite sides and free on the two other sides, as depicted in Figure 21.

The slabs were reinforced using bars with a diameter of 8 mm and a spacing of 50 mm, in each way and on each face. In the following calculation models it is assumed that the distance of the centre of rebars from the plate face is 19 mm. The effective plate thickness *d* becomes then 0.15 m - 0.019 m = 0.131 m. The reinforcement ratio is in this case $\rho_s = A_s/h$=0.0067.

Assuming f_c = 58 MPa, f_y = 560 MPa (a stress value obtained at 5 % strain value in the stress strain curve) the plastic moment capacity becomes $m_p = 0.0705$ MNm/m.

Assuming a shear cone angle of 35^0 the masses of the TDOF model become $m_1 = 69$ kg and $m_2 = 491$ kg when the effective mass is 560 kg. The stiffness

coefficients of the shear and bending springs are $k_s = 0.22 \cdot 10^{12}$ N/m and $k_b = 0.22 \cdot 10^{8}$ N/m, respectively.

The plastic limit load by the mechanism with one yield line crossing the plate, in Figure 21, is

$$F_p = 4m_p \frac{B}{L} = 3.636 m_p = 0.256 \text{ MN}. \tag{63}$$

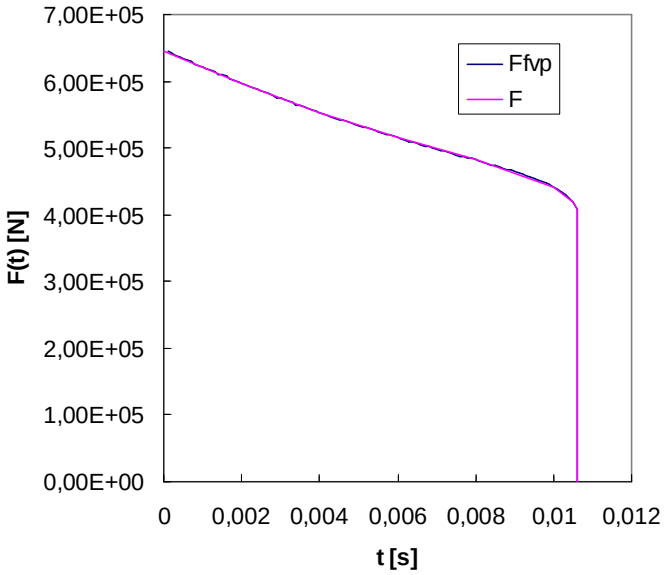

Figure 22. Load function due to dry aluminium missile in Test 642.

The internal plastic force of the bending spring is thus also $R_p = 0.256$ MN.

In calculating the equivalent mass of the SDOF and TDOF models an effective density of the slab is defined as

$$\rho_e = (1 - 4\rho_s)\rho_c + 4\rho_s\rho_{st} = (1 - 0.0268)2400 + 0.0268 \cdot 7850 = 2546 \text{ kg/m}^3 \tag{64}$$

where ρ_s = 0.67%=0.0067 is the reinforcement ratio, ρ_c = 2400 kg/m^3 and ρ_{st} = 7850 kg/m^3 are the assumed densities of concrete and steel, respectively. The equivalent mass becomes

$$m = \frac{M}{3} = \frac{0.15 \cdot 2.2 \cdot 2.0 \cdot 2546}{3} = 560 \text{ kg}, \tag{65}$$

where M is the mass of the slab.

The impact load due to an aluminium pipe missile is shown in Figure 22. Curve labelled F_{fvp} is calculated with the Riera method assuming a folding visco-plastic mechanism in calculating the crushing force P_c, [6]. The Cowper-Symonds visco-plastic power law type strain rate dependency is assumed for aluminium with parameter values

q = 4 and D = 6500. Curve F is a linear 9 point approximation of the actual force function to be used in calculations. The approximate force is diminishing from 0.645 MN to 0.408 MN during a time interval of 0.0106 s. The simplified load function corresponds to that obtained in Test 642 with a dry aluminium missile. The impulse of the load function is I = 5629 Ns.

A tentative finite element model solution curve DME is computed with Abaqus/Explicit [1] using the damaged plasticity model for concrete and an elastic visco-plastic strain hardening model for reinforcement assuming parameter values q = 5 and D = 40.4 1/s. The used plate element mesh is depicted in Figure 21. A layered plate model with an 11 point Simpson integration rule is used in the thickness direction. The modelling of concrete and reinforcing steel is described later in more detailed.

In Figure 23 the curve TDOF-D100 is calculated with damping coefficients ζ_1 =0.1 and ζ_2 =0. In this case shear deformation does not become active.

Force histories of TDOF plate model of test 642 with an impact velocity of v_0 = 109 m/s and angle of shear cone α=35^o are depicted in Figure 24.

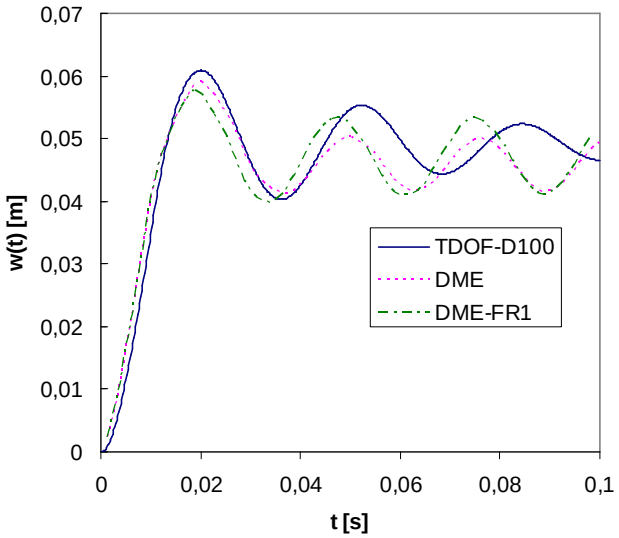

Figure 23.Deflection of plate in test 642. In case DME-FR1 the support frame (FR1) is modelled with beam elements.

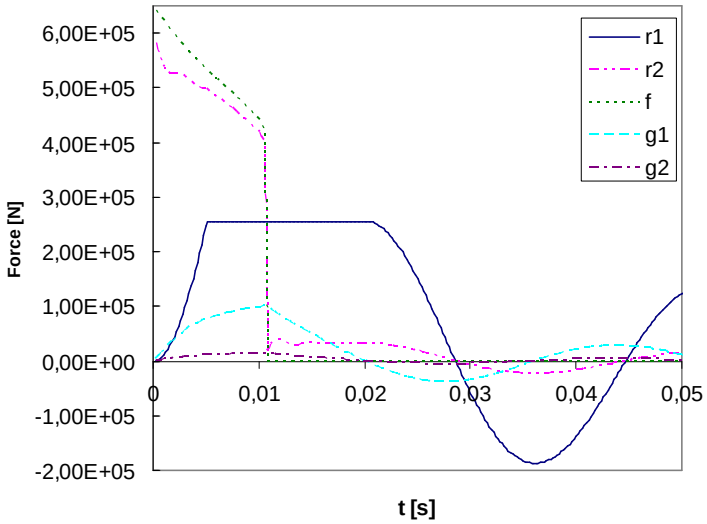

Figure 24. Forces of TDOF plate model of test 642, v_0=109 m/s, α=35^o.

Further finite element analyses

More detailed finite element analyses for the previous impact plate were carried out with Abaqus/Explicit. The finite element model for one quarter of the wall is shown in Figure 25. The reinforcement is modelled as layers in the four-noded shell elements. The loaded area is determined by assuming a load spreading angle of 45^o in the slab thickness direction to the shell mid surface. The load area is indicated by red colour.

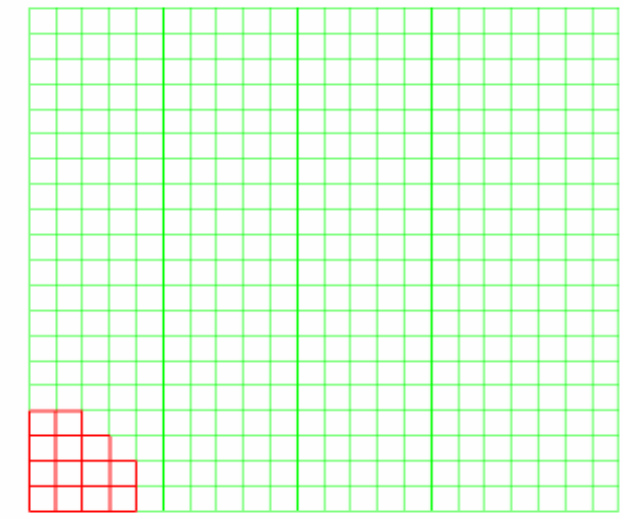

Figure25. One quarter finite element model of impact test walls.

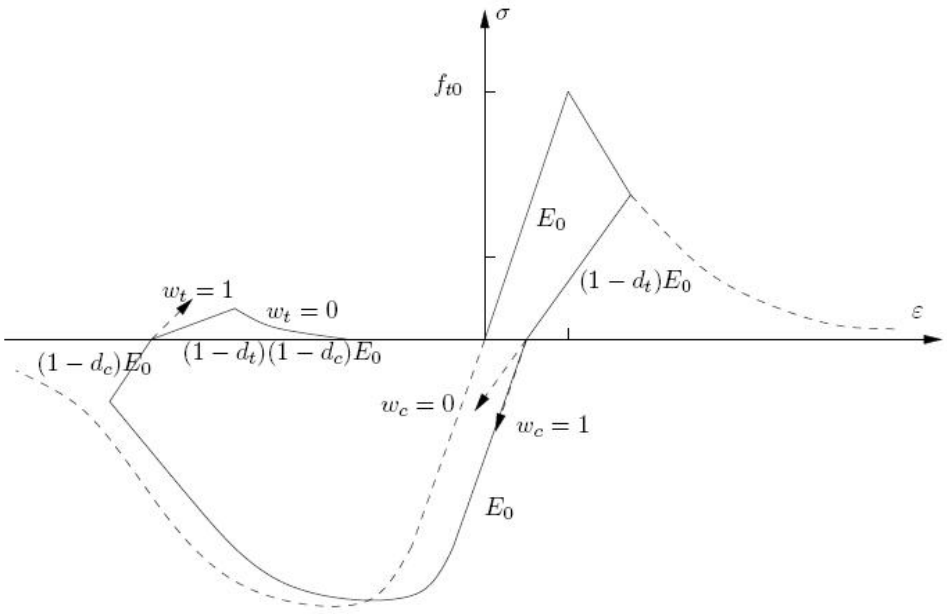

Figure 26. Uniaxial damage model of concrete in ABAQUS.

Damage plasticity material model for reinforced concrete

In a material model called *concrete damaged plasticity* in ABAQUS material degradation is taken into account in compression and tension. Damage is associated with cracking and crushing. In scalar damage theory the stiffness degradation is isotropic. Under uniaxial tension the stress-strain relationship is

$$\sigma_t = (1-d_t)E_0(\varepsilon_t - \bar{\varepsilon}_t^p), \tag{66}$$

where E_o is the undamaged modulus of elasticity, d_t is tension damage scalar variable, $\bar{\varepsilon}_t^p$ is the equivalent plastic strain in tension. In compression, correspondingly,

$$\sigma_c = (1-d_c)E_0(\varepsilon_c - \bar{\varepsilon}_c^p), \tag{67}$$

where d_c is compression damage scalar variable.

Compressive stiffness is recovered upon crack closure as the load changes from tension to compression, but the tensile stiffness is not recovered when the load changes from compression to tension. In Figure 26 *wt* = 0 corresponds to no recovery as load changes from compression to tension and *wt = 1* corresponds to complete recovery as the load changes from tension to compression.

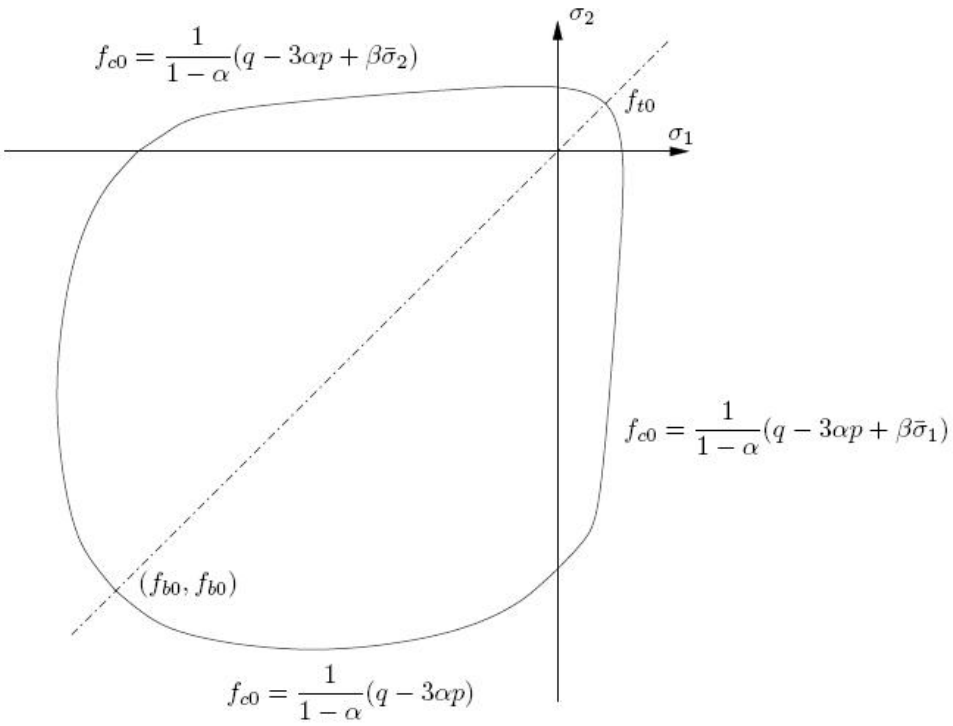

Figure 27. Yield surface in plane.

The biaxial yield function is combined of two Drucker-Prager type functions. In Figure 27 α is a coefficient

$$\alpha = \frac{f_{b0} - f_{c0}}{2 f_{b0} - f_{c0}}, \quad 0 \le \alpha \le 0.5, \tag{68}$$

where f_{c0} is the initial uniaxial compressive yield stress, f_{b0} is the initial equibiaxial compressive yield stress, f_{t0} is the uniaxial tensile stress at failure, p is the hydrostatic pressure stress,

$$p = -\frac{I_1}{3} = -\frac{\sigma_{11} + \sigma_{22} + \sigma_{33}}{3}, \tag{69}$$

q is the effective von Mises stress

$$q = \sqrt{3J_2}, \tag{70}$$

J_2 is the second deviatoric stress invariant

$$J_2 = \frac{1}{2} S_{ij} S_{ij} \quad , \tag{71}$$

where the deviatoric stress is

$$S_{ij} = \sigma_{ij} - \frac{\sigma_{kk}}{3}\delta_{ij}, \quad \delta_{ij} = \begin{Bmatrix} 1 & \text{if, i = j} \\ 0 & \text{if, i} \neq \text{j} \end{Bmatrix}, \tag{72}$$

in biaxial loading

$$J_2 = \sigma_{11}^2 + \sigma_{22}^2 - \sigma_{11}\sigma_{22}, \tag{73}$$

β is a dimensionless coefficient

$$\beta = \frac{\bar{\sigma}_c(\bar{\varepsilon}_c^p)}{\bar{\sigma}_t(\bar{\varepsilon}_t^p)}(\alpha - 1) - (\alpha + 1), \tag{74}$$

$\bar{\sigma}_c$ is the effective compressive cohesion stress, $\bar{\sigma}_t$ is the effective tensile cohesion stress.

The Drucker-Prager plastic potential function is shown in Figure 28.

$$G = \sqrt{(\varepsilon f_{t0} \tan\psi)^2 + q^2} - p\tan\psi, \tag{75}$$

where ε is an eccentricity coefficient and ψ is the dilatation angle, in (p,q)-plane, at high confining pressure. In the present calculation $\psi = 36.3^{\circ}$ is assumed and usually $\varepsilon = 0.1$.

The plastic strain is according the normality principle

$$d\varepsilon_{ij}^p = \lambda \frac{\partial G}{\partial \sigma_{ij}}, \tag{76}$$

where λ is a proportionally coefficient, see Figure 28.

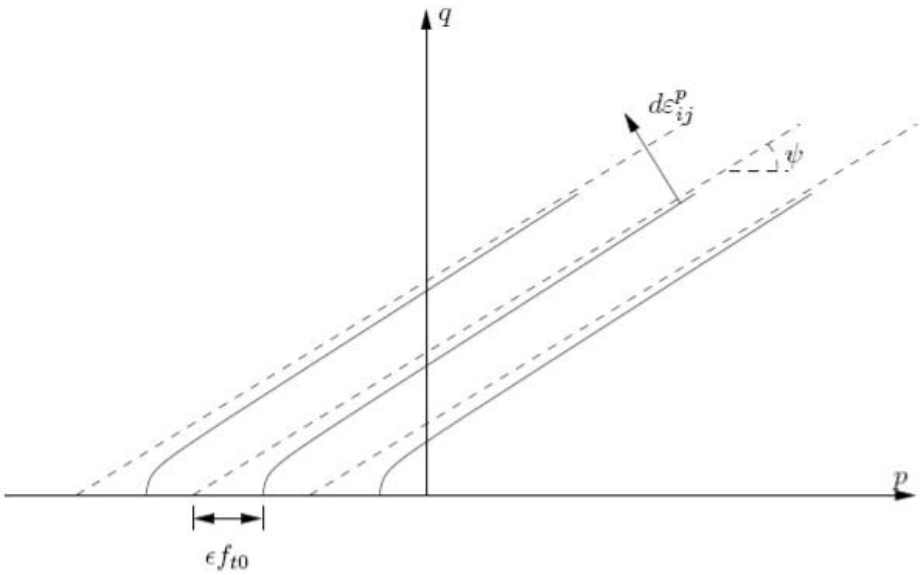

Figure 28. Potential function.

The measured ultimate compression crushing strength of the concrete material is 58 MPa. The assumed compression stress as a function of strain is shown in Figure 29. In the following analyses, if not otherwise mentioned, this compression crushing curve is applied.

The smeared stress-strain curve of concrete in tension can be defined as

$$\sigma_1 = E_c \varepsilon_1, \ \varepsilon_1 \le \varepsilon_{cr} \tag{77}$$

and

$$\sigma_1 = f_{cr} \left(\frac{\varepsilon_{cr}}{\varepsilon_1} \right)^{0.4}, \ \varepsilon_1 > \varepsilon_{cr}, \tag{78}$$

where E_c is the modulus of elasticity of concrete, f_{cr} is the cracking stress of concrete and ε_{cr} is the cracking strain of concrete [12].

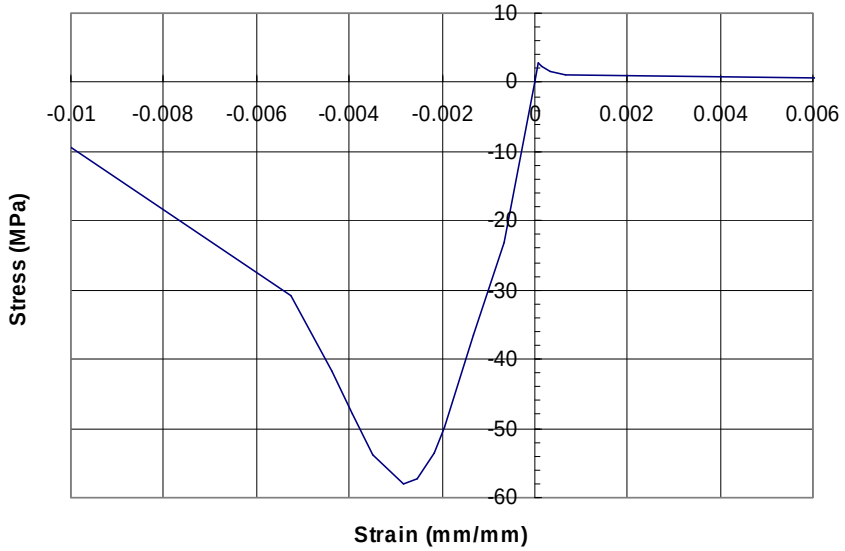

Figure 29. Uniaxial stress-strain curve for concrete.

Nonlinear tensile stress-strain curves predicted according to the method in Reference [12] using the measured tensile splitting strength values are presented in Figure 30. These curves were further modified by setting the tensile strength to zero, when the tensile strain reaches the value of 0.67%. Results calculated with this assumption are referred to as f_{ctk_zero}.

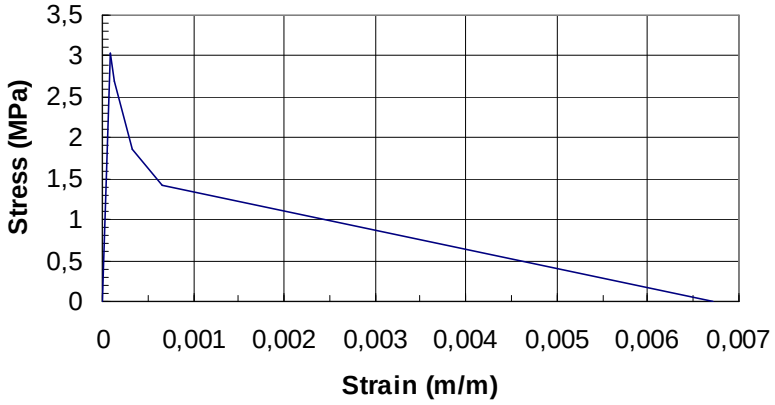

Figure 30. Tensile stress-strain behavior of concrete material model.

The use of the average (smeared) steel stresses in combination with the corresponding concrete stresses allows the tension stiffening effect (of steel bars by concrete) to be considered and deformations of the steel concrete composites to be correctly evaluated [12]. The stress in reinforcement is

$$\sigma_s = E_s \varepsilon_s, \ \ \varepsilon_s \le \varepsilon_y \tag{79}$$

and

$$\sigma_s = f_y[(0.91-2B)+(0.02+0.25B\frac{\varepsilon_s}{\varepsilon_y})], \ \ \varepsilon_s > \varepsilon_y \tag{80}$$

where σ_s and ε_s are the average (smeared) stress and strain of mild steel bars in concrete, f_y and ε_y are the yield stress and strain of mild steel bars in concrete, E_s is the modulus of elasticity of reinforcement. The parameter B is defined by the formula

$$B = \frac{1}{\rho}\left(\frac{\sigma_{cr}}{\sigma_y}\right)^{1.5}, \tag{81}$$

where the reinforcement ratio ρ is greater than 0.5 %.

The stress-strain curves for reinforcement used in the nonlinear analyses are presented in Figure 31.

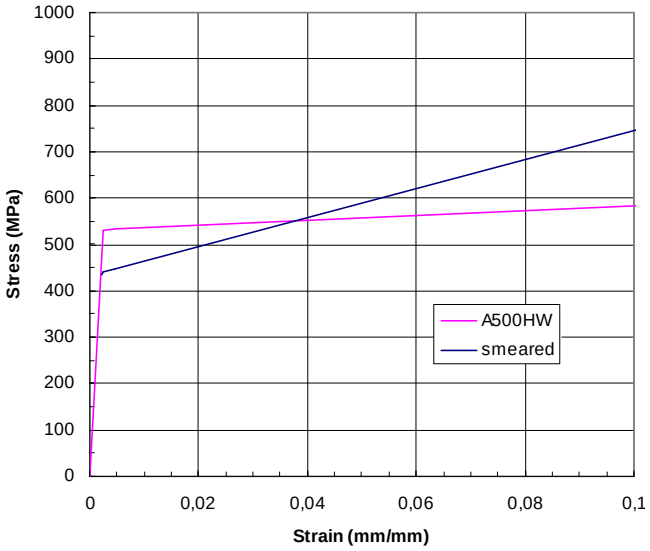

Figure 31. Stress-strain dependency for reinforcement steel.

The yield strength of reinforcement steel is highly strain rate dependent and increases with the strain rate. This dynamic yield strength of steel was taken into consideration by the Cowper-Symonds formula for uniaxial tension or compression.

Deflections calculated with tensile stress–strain dependency, presented in Figures 30 and 31, are shown with the corresponding measured data in Figure 32. The calculated deflections (dotted lines) are still quite close to the measured values, though they are somewhat larger than the displacements presented above.

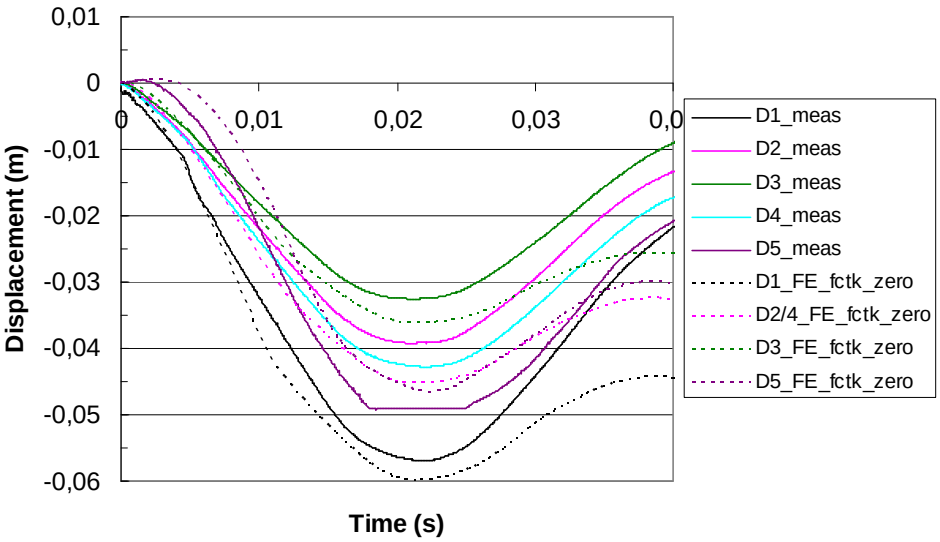

Figure 32. Measured and calculated deflections in Test 642.

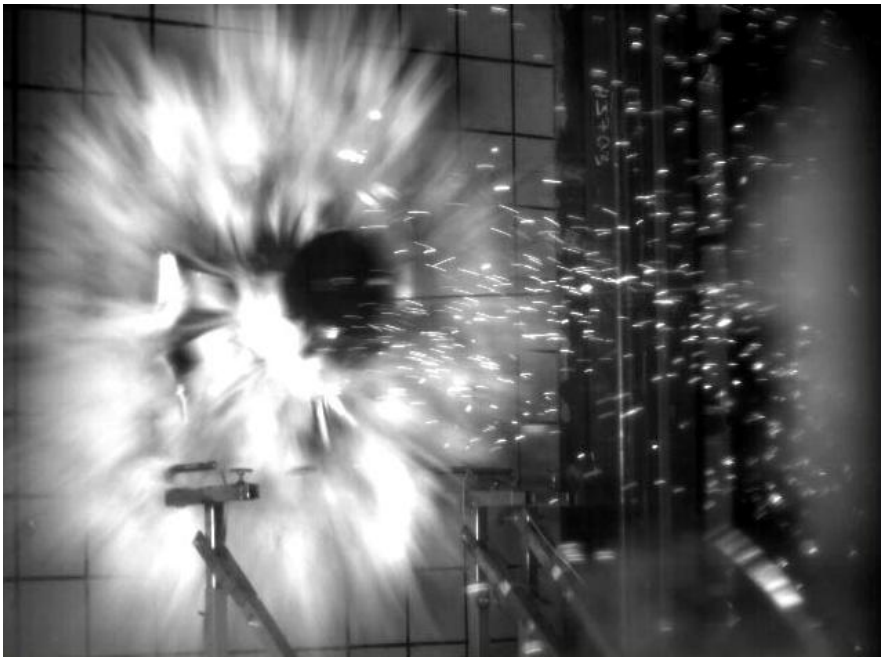

Figure 33. Typical liquid plash pattern from a cylindrical (left) and a prototypical 3D missile (right).

Liquid spreading

The main aim of the liquid spreading studies was to get quantitative data detailed enough to be utilised in the validation of the simulation methods (FDS code) that are to be used for determination of fuel spread and fire risk following an airplane crash.

The speed and direction of liquid spray coming out from a ruptured missile is measured using a high-speed video camera (1000 fps). Figure 33 shows a typical splash pattern around a cylindrical (left) missile. The deceleration of the missile is very rapid in impact, and consequently, liquid spurts out from the missile when the liquid container fails resulting in dispersal around the target. In case of cylindrical missile, the liquid release starts along the surface quite perpendicularly to the missile direction, and forms a fairly "flat" and uniform circular splash pattern. The pattern becomes thicker as the breakup of the liquid core begins. According to the measurements, the initial discharge speed of the liquid is in some cases even as high as 2.5 times the impact velocity of the missile, but the propagation speed of the spray front decreases rapidly when the distance from the impact target increases. The furthest splashes found on the floor were located about 15 meters sidewards from the impact target.

A typical propagation speed of a liquid (spray) front coming out from the cylindrical missile with associated deceleration can be seen in Figure 35. Also two simulation results of the FDS program with different droplet initial median diameter are shown. The impact velocity in the test was 125 m/s and the initial discharge velocity of liquid was about 250 m/s. The x-axis of the Figure 34 indicates the distance from the missile meanwhile the y-axis shows the ratio of liquid velocity to its initial velocity. Within 1.5 meters distance from the impact target, the speed of the liquid front decreases to a value which is about half of the initial speed. The FDS simulation with a 300 µm median droplet diameter yields good results comparing to the experimental data.

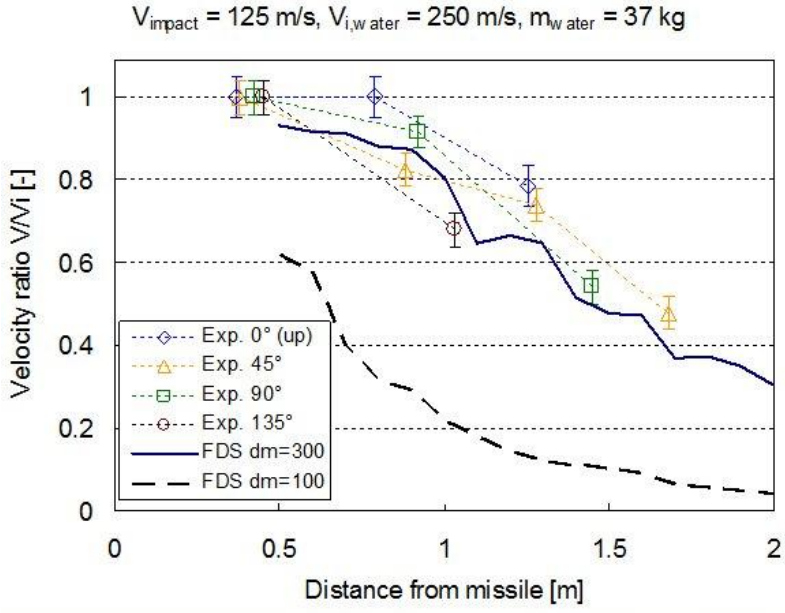

Figure 34. Measured and simulated speed of liquid front in an IMPACT test.

Fire dynamic simulations

Feasibility of the FDS for the simulation of fire due to an impact was studied by modifying the previously studied scenario. The purpose of the work was to find out whether FDS can be used for the simulation of such a rapid fire resulting from a sudden release of small, fast moving fuel droplets. The simulations were made in the scale of Impact tests, Figure 35. The results of the simulation included the qualitative behaviour, heat fluxes to the surrounding surfaces and the mass of the non-burned fuel droplets forming a pool fire.

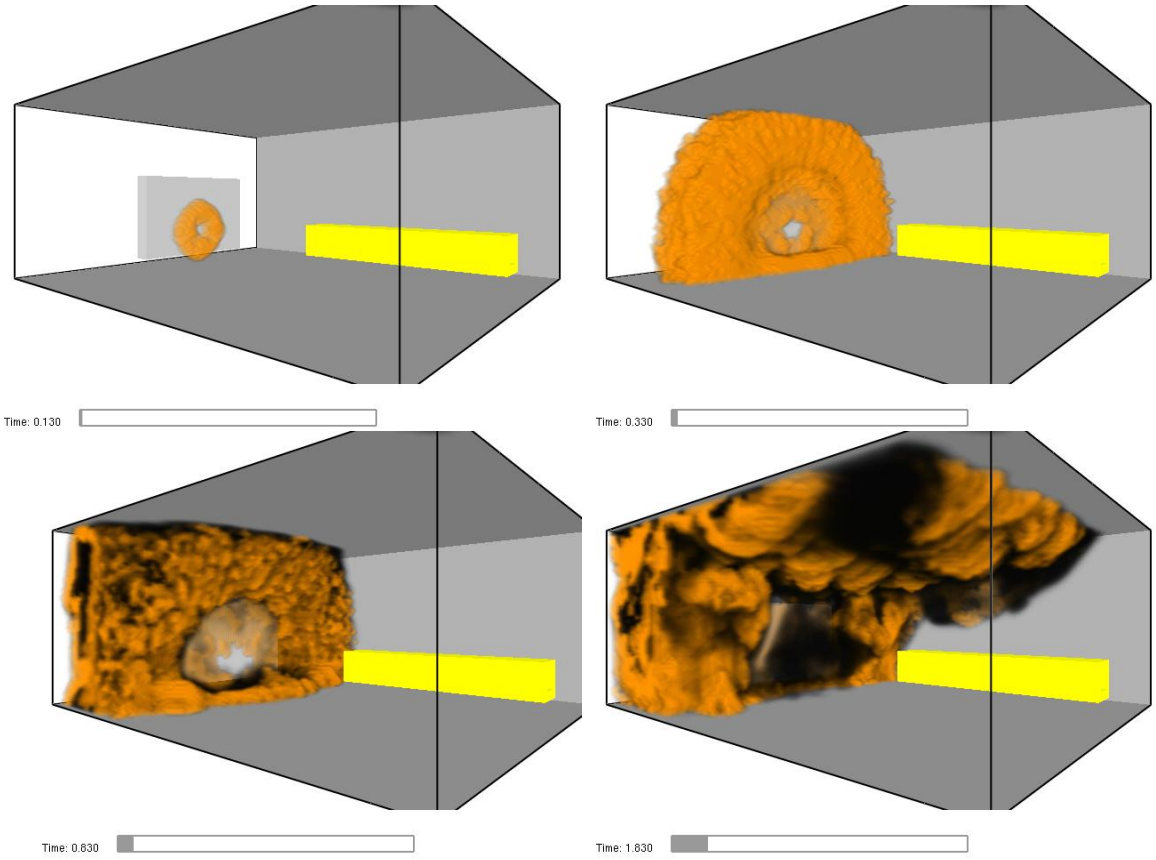

Figure 35. Development of the flame.

The results of the preliminary simulations with FDS code show that it is a usable tool in simulating the two-phase flows involving high-speed droplets provided that initial conditions (angle and velocity of liquid release, droplet size distribution and air speed) can be specified satisfactory. Given that, the formation of the water cloud and final water distribution is predicted by FDS reasonably well.

Also, the simulation results of liquid fuel dispersal and burning were both qualitatively and quantitatively plausible, although the actual uncertainties are difficult to estimate.

Discussion and Conclusions

Many tests have been done successfully with the Impact test facility and the test campaign is now moving towards more complex and more elaborate, 3D missile designs. Some 15 tests are conducted with fluid filled missiles giving valuable information on liquid speed, drop size, and dispersal phenomena under impact conditions. Also the simulation capabilities (Fire Dynamics Simulator (FDS) software) for liquid spreading and fire studies have been taken in use and developed.

Bending or shear failure of a reinforced concrete slab subjected to a projectile impact can be simply modelled with a two mass system. The two mass system is, however, sensitive to the assumed angle of shear failure cone. Before developing a simplified method capable of predicting the shear fracture angle parametric 3D-finite element analyses can be used for estimating a plausible value for shear cone angle. Also experimental findings can be used in defining the shear angle for different kind of slabs and load cases. The determination of proper damping parameters requires carefully conducted experiments.

Based on these studies it can be concluded that the used shell element models with simple four noded element where the transverse nonlinear shear deformation is not considered are capable for calculating the deflection behaviour of a reinforced concrete wall representing a full scale model loaded by a deformable missile. Nonlinear analyses of reinforced structures are quite sensitive for material parameters, however. Especially, in the case where the wall is rather weakly reinforced the tensile cracking properties of concrete dominate the nonlinear bending behaviour of the wall.

The experimental findings indicate that the liquid release starts along the surface quite perpendicularly to the incoming direction of the missile and forms a fairly flat splash pattern. The initial discharge speed of the liquid front coming out of the ruptured missile may be much higher than the impact velocity of the missile, but the propagation speed of the spray front decreases rapidly when the distance from the source increases.

The results of the preliminary simulations with FDS code show that it is a usable tool in simulating the two-phase flows involving high-speed droplets provided that initial conditions (angle and velocity of liquid release, droplet size distribution and air speed) can be specified satisfactory. Given that, the formation of the water cloud and final water distribution is predicted by FDS reasonably well.

Also, the simulation results of liquid fuel dispersal and burning were both qualitatively and quantitatively plausible, although the actual uncertainties are difficult to estimate.

Acknowledgements

The authors wish to thank the following colleagues for their contribution to this work: Tuomo Kärnä, Auli Lastunen, Jukka Mäkinen, Juha Juntunen, Erkki Järvinen, Matti Halonen, Leo Lapinluoma and Jouni Hietalahti.

Numerical studies and Liquid dispersal studies have been carried out within the SUSI –project (Structures Under Soft Impact) and all the tests were carried out within the IMPACT project in the Finnish Research Programme on Nuclear Power Plant Safety SAFIR2010. Both projects have been funded by the State Nuclear Waste Management Fund (VYR) and by VTT. The contribution of the ad hoc group is greatly acknowledged.

References

[1] Abaqus Theory Manual, Version 6.7, SIMULIA, Dassault Systemes, 2007.
[2] Riera J.D. On the stress analysis of structures subjected to aircraft impact forces. *Nuclear Engineering and Design*, Vol 8 (1968) pp. 415-426.
[3] Kuutti J., Design of Projectile for Impact testing. Master Thesis, Helsinki University of Technology, 2007.
[4] Abbas H., Paul D.K., Godbole P.N. and Nayak G.C. Soft missile impact on rigid targets. *International Journal of Impact Engineering*, Vol 16, 1995, 727-737.
[5] Drittler K., Gruner P. and Krivy J., Calculation of forces arising from impacting projectiles upon yielding structures. The 4th International Conference on Structural Mechanics in Reactor Technology, Paper J7/4, 1977, 1-12.
[6] Alexander J.M., An approximate analysis of the collapse of thin cylindrical shells under axial loading. *Quarterly Journal of Mechanics and Applied Mathematics*, Vol 13, 1960, 10-15.
[7] Jones, N. (1989), Structural Impact. Cambridge University Press, 1989.
[8] Sugano T., Tsubota H., Kasai Y., Koshika N., Orui S., von Rieseman W.A., Bickel D.C. and Parks M.B., (1993 a), Full-scale aircraft impact test for evaluation of impact force. *Nuclear Eng. and Design*, Vol 140, 1993, 373-385.
[9] Sugano T., Tsubota H., Kasai Y., Koshika N., Ohnuma H., von Rieseman W.A., Bickel D.C. and Parks M.B., (1993 b), Local damage to reinforced concrete structures caused by impact of aircraft engine missiles. Part 1. Test program, method and results. Nuclear Engineering and Design, Vol 140, 1993, 387-405.
[10] Sugano T., Tsubota H., Kasai Y., Koshika N., Itoh H., Shirai K., von Rieseman W.A., Bickel D.C. and Parks M.B., (1993 c), Local damage to reinforced concrete structures caused by impact of aircraft engine missiles. Part 2. Evaluation of test results. *Nuclear Engineering and Design*, Vol 140, 1993, 407-423.
[11] CEB Bulletin d'Information no. 187. 1988. Concrete Structures under Impact and Impulsive Loading.
[12] Wang, T. and Hsu, T. 2001. Nonlinear Finite Element analysis of concrete structures using new constitutive models. *Computers & Structures* vol. 79, 2001, pp. 2781-2791.

Arja Saarenheimo, Kim Calonius, Ilkka Hakola, Simo Hostikka and Ari Silde
VTT Technical Research Centre of Finland,
P.O.Box 1000, FI-02044 VTT, Finland, arja.saarenheimo@vtt.fi

Markku Tuomala
Tampere University of Technology
P.O.Box 600, 33101 Tampere, Finland, markku.tuomala@tut.fi